

SURE-Med: Systematic Uncertainty Reduction for Enhanced Reliability in Medical Report Generation

Yuhang Gu¹, Peng Peng², Xingyu Hu³, Yuyu Fan¹, Xuling Yan¹, Longhuan Xu¹

¹School of Biomedical Engineering, Southeast University, Nanjing, China

²Zhejiang University, Hangzhou, China

³Georgia Institute of Technology, USA

Abstract

Automated medical report generation (MRG) holds great promise for reducing the heavy workload of radiologists. However, its clinical deployment is hindered by three major sources of uncertainty. First, visual uncertainty, caused by noisy or incorrect view annotations, compromises feature extraction. Second, label distribution uncertainty, stemming from long-tailed disease prevalence, biases models against rare but clinically critical conditions. Third, contextual uncertainty, introduced by unverified historical reports, often leads to factual hallucinations. These challenges collectively limit the reliability and clinical trustworthiness of MRG systems. To address these issues, we propose SURE-Med, the first unified framework that systematically reduces uncertainty across three critical dimensions—visual, distributional, and contextual. To mitigate visual uncertainty, a Frontal-Aware View-Repair Resampling module corrects view annotation errors and adaptively selects informative features from supplementary views. To tackle label distribution uncertainty, we introduce a Token-Sensitive Learning objective that enhances the modeling of critical diagnostic sentences while reweighting underrepresented diagnostic terms, thereby improving sensitivity to infrequent conditions. To reduce contextual uncertainty, our Contextual Evidence Filter validates and selectively incorporates prior information that aligns with the current image, effectively suppressing hallucinations. Extensive experiments on the MIMIC-CXR and IU-Xray benchmarks demonstrate that SURE-Med achieves state-of-the-art performance. By holistically reducing uncertainty across multiple input modalities, SURE-Med sets a new benchmark for reliability in medical report generation and offers a robust step toward trustworthy clinical decision support.

Code — <https://anonymous.4open.science/r/test-mc/>

Introduction

Chest X-ray (CXR) is among the most widely used imaging modalities in clinical practice, offering critical diagnostic information on the lungs, heart, pleura, and bones. It is essential for detecting and assessing thoracic diseases such as pneumonia, pneumothorax, pleural effusion, fractures, and cardiomegaly. However, CXR interpretation and radiology report composition remain manual tasks, which are both expertise-dependent and time-consuming (Liu et al.

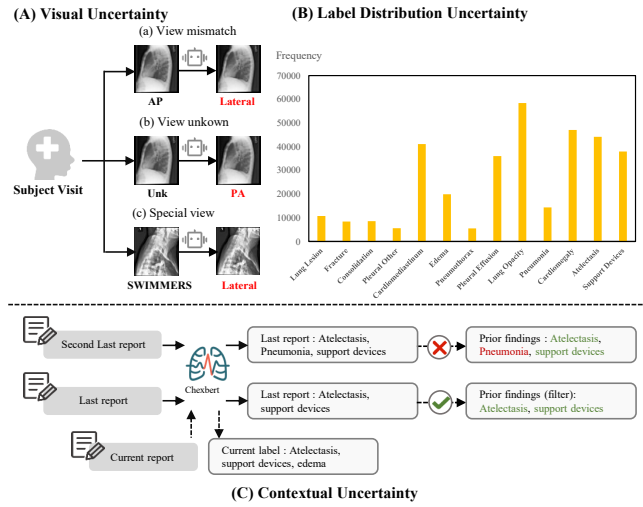


Figure 1: Three key sources of uncertainty in medical report generation: (A) Visual: view mismatches or unknown/special views. (B) Label distribution: long-tailed diagnostic frequency. (C) Contextual: inconsistent prior reports (filtered to reduce noise).

2024b; Wang et al. 2025a). With imaging volumes increasing, the reporting burden is becoming unsustainable, potentially compromising clinical efficiency and patient care (Wang, Du, and Yu 2025; Bannur et al. 2024). Radiology Report Generation (RRG) has emerged as a promising automated solution (Jing, Xie, and Xing 2018). RRG models generate structured, coherent clinical narratives by interpreting various imaging modalities—such as CXRs (Liu et al. 2024d), computed tomography (CT) (Hamamci, Er, and Menze 2024), and pathology slides (Guo et al. 2024)—using data-driven natural language processing techniques. By producing high-quality draft reports, these systems streamline radiologists' workflows, reduce reporting latency, and enhance documentation consistency (Tanno et al. 2025; Wang et al. 2023a).

Among various projection techniques, the posteroanterior (PA) view offers the most comprehensive visualization of lung fields and mediastinal structures, forming the cornerstone of routine chest radiograph (CXR) interpretation

(Broder 2011). PA imaging is preferred due to its perpendicular beam and minimal heart-to-detector distance, which reduces cardiac magnification and enhances the detection of subtle pulmonary lesions (Simkus et al. 2021; Gupte et al. 2021). When PA imaging is not feasible, the anteroposterior (AP) view is employed, though it is compromised by cardiac magnification and suboptimal lung inflation, which may produce pseudolesions (Amorosa et al. 2013). Lateral and oblique views complement frontal projections by aiding lesion localization and improving contrast in overlapping structures. Consequently, the PA view remains central to reliable cardiopulmonary assessment and underpins most diagnostic interpretations.

Accurate view annotations are critical for the performance of AI-based RRG systems. However, nearly one-third of studies are excluded due to missing or ambiguous PA/AP labels (Gaggion et al. 2024). Similarly, (Liu et al. 2025a) reported comparable issues and proposed learnable vectors for “unknown” and “special” view tags to mitigate misclassification risks.

Beyond view annotation errors, additional data quality challenges constrain RRG reliability. Class imbalance—where common findings dominate while rare but critical conditions are underrepresented—biases models toward frequent diseases (Jin et al. 2024). Historical free-text reports introduce hallucinated findings (Ramesh, Chi, and Rajpurkar 2022) and non-clinical content (Nguyen et al. 2023), and the reliability of earlier time points declines over time; although they provide valuable historical context, this can dilute the supervision signal and slow model convergence. Collectively, these challenges manifest as three principal sources of uncertainty—(1) visual uncertainty due to noisy or missing view annotations, (2) label distribution uncertainty caused by severe class imbalance, and (3) contextual uncertainty arising from unreliable or misleading prior reports—as illustrated in Fig. 1.

Inspired by these observations, we present SURE-Med, a unified uncertainty-reduction framework for radiology report generation that systematically addresses the three dominant sources of uncertainty—visual, label distribution, and contextual. SURE-Med comprises three core modules, each targeting a specific type of uncertainty: frontal-aware view-repair resampling (FAVR) to mitigate visual uncertainty, token-sensitive learning (TSL) to address label distribution uncertainty, and contextual evidence filter (CEF) to reduce contextual uncertainty. In FAVR, we automatically correct view mismatches, resolve unknown view tags, and normalize special projections into coherent frontal and lateral views. In TSL, we apply a token-level data-imbalance augmentation strategy to upweight underrepresented pathology statements—ensuring the model focuses on critical diagnoses and small-sample findings. In CEF, we filter historical report segments by similarity to remove low-confidence content, then apply a stricter cutoff to the second-to-last report—retaining only high-confidence findings—to leverage multi-time-point evidence while minimizing outdated noise and ensuring factual consistency. The contributions of our work are outlined as follows:

- We introduce a FAVR module to correct view-annotation

errors, thereby providing cleaner inputs that enable our frontal-guided resampler to extract features more effectively. We have also released a more robust view-repair dataset to support the correction of view annotation errors, helping reduce visual uncertainty in multimodal chest X-ray tasks.

- We propose a TSL strategy that dynamically upweights underrepresented pathology tokens to strengthen the model’s focus on key diagnostic phrases, thereby mitigating data-imbalance bias.
- We introduce a CEF to dynamically screen prior report text, reducing model hallucination and improving factual accuracy. The filter preserves clinically essential content and fully leverages multi-time-point evidence to capture disease progression.
- Experimental evaluations of SURE-Med were conducted on two public datasets, MIMIC-CXR and IU-Xray. The results demonstrate that SURE-Med outperforms state-of-the-art methods across various evaluation metrics.

Related Works

Radiology report generation

Radiology report generation extends the paradigm of image captioning (Zeng et al. 2023) by requiring detailed, terminology-rich diagnostic text. Mostly systems adopt an encoder-decoder scheme—borrowed from Xu et al. (2015), Lu et al. (2017), and Ji et al. (2021)—that couples a visual backbone (e.g. ResNet101(Chen et al. 2021; Huang, Zhang, and Zhang 2023), CvT(Nicolson, Dowling, and Koopman 2023), or ViT(Liu et al. 2024e)) with a language model (e.g. Memory-driven Transformer(Chen et al. 2020; Liu et al. 2024c), MiniGPT4(Liu et al. 2024a), DistilGPT2(Nicolson, Dowling, and Koopman 2023; Jin et al. 2024; Liu et al. 2025a)). To boost clinical reliability, researchers have infused domain knowledge via knowledge graphs (Zhang et al. 2020; Yang et al. 2022), cross-modal alignment methods (Chen et al. 2024a; Liu et al. 2024c), region-aware network designs (Zhao, Yan, and Zhao 2023; Zhang et al. 2024), warm-start initialization (Nicolson, Dowling, and Koopman 2023) and temporal progression models (Yang et al. 2024; Wang, Du, and Yu 2024). Yet most recent studies process only a single view, overlooking the complementary information from multiple projections and failing to address view-label errors. In this work, we introduce SURE-Med, which leverages a multi-view strategy where the frontal (PA/AP) view guides feature extraction from lateral projections. Furthermore, we incorporate a view-label correction module to mitigate visual uncertainty, thereby enhancing the clinical reliability of chest X-ray report generation.

Data Imbalance and Token-Level Enhancement

Medical imaging datasets, particularly chest X-ray repositories, exhibit pronounced long-tailed distributions: a few common findings (e.g., “No Finding,” “Pleural Effusion”) account for the majority of samples, while most pathologies appear in less than 1% of images (Johnson et al. 2019;

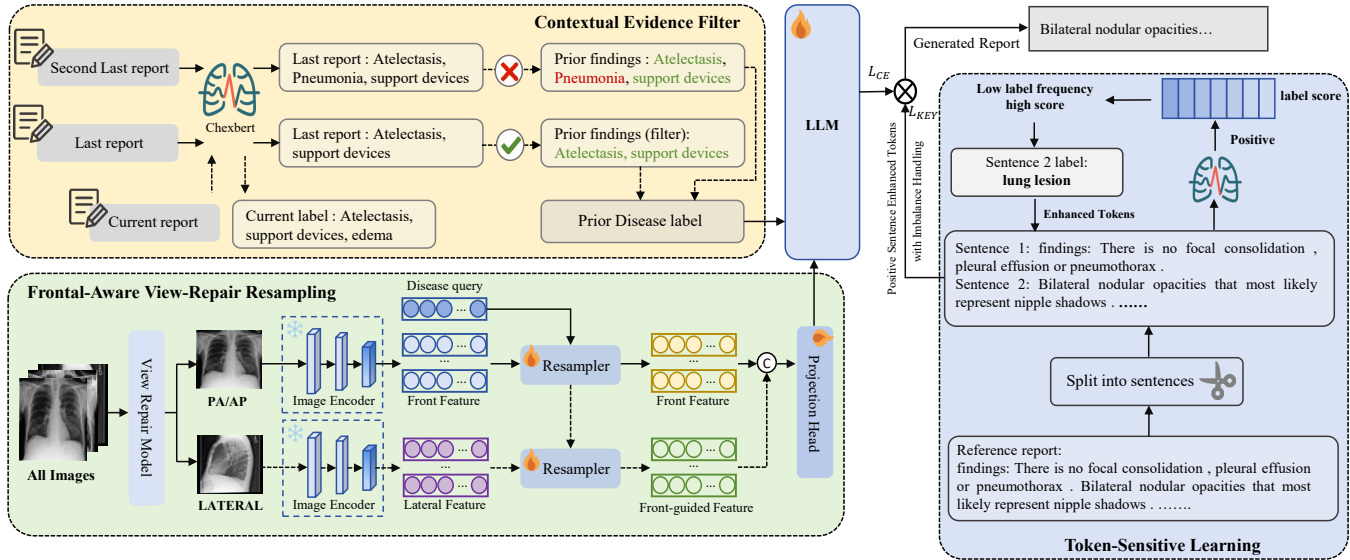


Figure 2: SURE-Med overview: (1) Contextual Evidence Filter extracts and filters prior findings from historical reports; (2) Front-Aware View-Repair Resampling recovers missing PA/AP and lateral labels and fuses multi-view features; (3) Token-Sensitive Learning amplifies key disease prompts to guide imbalance-aware generation of accurate radiology reports.

Holste et al. 2023). Typical mitigation strategies include minority oversampling via SMOTE (Chawla et al. 2002), Focal Loss (Lin et al. 2017), and class-balanced reweighting (Cui et al. 2019). In the medical domain, Rajpurkar et al. 2017 demonstrated that a weighted cross-entropy loss atop a deep CNN (CheXNet) can achieve radiologist-level pneumonia detection. Seo et al. 2023 extended balanced sampling strategies, which led to a marked improvement in detecting rare pathologies. PromptMRG reframes classification outputs as structured prompts—injecting disease labels and diagnostic cues directly into the generation pipeline—which significantly boosts clinical relevance metrics and reduces hallucinated content in the resulting reports (Jin et al. 2024). However, all of these interventions operate at the level of images or label categories and do not directly guide the language model to generate clinically critical sentences nor enhance its sensitivity to rare conditions. To address this shortfall, we introduce a token-level data-imbalance mechanism that not only bolsters the model’s ability to generate clinically critical sentences but also heightens its sensitivity to rare conditions.

Enhancing medical image analysis via longitudinal data

Longitudinal data enable models to capture disease evolution over multiple time points. Prior work has directly integrated historical images and reports into the generation pipeline: CXRMATE(Nicolson et al. 2024) synthesizes previous studies’ reports from past images and feeds them alongside current multi-view images to produce the final diagnosis text; MLRG(Liu et al. 2025a) uses past images as a retrieval corpus, combining them with current images and auxiliary views for cross-time modeling, and directly injects encoded historical report features into the decoder. Although

these methods leverage longitudinal information, they can inadvertently introduce hallucinated content that does not match the current image. To mitigate this, we propose a dynamic historical report filtering mechanism: We score and select only high-confidence prior-study entries that semantically align with the current image, enabling the model to use longitudinal data more precisely and substantially reducing hallucinations from irrelevant or outdated findings.

Method

The overall architecture, depicted in Figure 2, consists of three primary components: FAVR, CEF and TSL. The FAVR corrects view labels using a pretrained classifier, extracts features from all views with a shared encoder, and employs a fixed-length frontal token to guide lateral feature selection. The CEF encodes prior report segments and filters them by semantic similarity to the current image, retaining only high-confidence findings. The TSL upweights critical diagnostic tokens in report generation and incorporates data-imbalance mitigation to boost sensitivity to rare conditions.

Problem Formulation

Let the training set be $\mathcal{D}_{\text{tr}} = \{(X_i^{\text{cur}}, y_i^{\text{cur}}, y_i^{\text{pri1}}, y_i^{\text{pri2}})\}_{i=1}^n$, where each visit i contains a variable number m_i of current multi-view chest X-ray images $X_i^{\text{cur}} = \{x_{i,1}^{\text{cur}}, \dots, x_{i,m_i}^{\text{cur}}\}$, a reference report y_i^{cur} , and up to two prior reports y_i^{pri1} and y_i^{pri2} (either may be absent). Our goal is to learn a mapping $F_{\theta}(X_i^{\text{cur}}, y_i^{\text{pri1}}, y_i^{\text{pri2}}) \rightarrow y_i^{\text{cur}}$, enabling the generation of accurate radiology reports conditioned on available current images and existing prior reports, while robustly accommodating missing historical information.

Frontal-Aware View-Repair Resampling

Continuing from our problem formulation, we first apply a pretrained view-classifier model to split the current multi-view set X_i^{cur} into frontal images X_i^f and lateral images X_i^ℓ . Both subsets are passed through a frozen vision encoder E_v to produce visual token sequences:

$$H_i^f = E_v(X_i^f) \in \mathbb{R}^{N_i \times D} \quad (1)$$

$$H_i^\ell = E_v(X_i^\ell) \in \mathbb{R}^{N_i \times D} \quad (2)$$

where D is the feature dimension and N_i the number of tokens per view. We introduce learnable disease query tokens $V' \in \mathbb{R}^{N_q \times D}$, which serve as the queries for our frontal-view resampler r_f :

$$T^f = r_f(H_i^f, V') \in \mathbb{R}^{N_q \times D} \quad (3)$$

and then reuse these tokens to guide lateral-view resampling r_l :

$$T^\ell = r_l(H_i^\ell, T^f) \in \mathbb{R}^{N_q \times D} \quad (4)$$

Finally, we concatenate T^f and T^ℓ along the token dimension and project to a fixed output size d via

$$Z_i = P_v([T^f; T^\ell]) \in \mathbb{R}^{N_q \times d} \quad (5)$$

where $P_v(\cdot)$ is a lightweight projection head. The fused feature Z_i is then forwarded to the report decoder.

Token-Sensitive Learning

To emphasize rare but clinically important findings during training, we assign higher weights to sentences that contain low-frequency disease labels. For each key diagnostic sentence $s_{i,k}$, we collect the set of disease labels $\mathcal{J}_{i,k}$ marked as positive or uncertain by CheXbert. We then look up the frequency f_j of each label $j \in \mathcal{J}_{i,k}$ in the MIMIC-CXR training set, and determine the sentence rarity based on the least frequent label it contains. We then assign each sentence a raw weight

$$w_{i,k}^{\text{raw}} = \begin{cases} 1.0, & f_j \geq T_1 \\ 1.5, & T_2 \leq f_j < T_1 \\ 2.0, & f_j < T_2 \end{cases} \quad (6)$$

with thresholds T_1 (high frequency) and T_2 (mid frequency). Because key diagnostic sentences represent only a small fraction of the report, applying raw weights directly would concentrate extremely large gradients on rare sentences and nearly zero on the rest, risking gradient explosion and training instability. To mitigate this, we normalize the raw weights into $[\alpha, 1]$ as follows:

$$M = \max_{i,k} w_{i,k}^{\text{raw}} \quad (7)$$

$$w_{i,k} = \alpha + (1 - \alpha) \frac{w_{i,k}^{\text{raw}}}{M} \in [\alpha, 1] \quad (8)$$

Here, setting $\alpha = 0.1$ ensures that even the most common sentences receive some gradient signal, while capping the maximum at 1.0 prevents extreme updates.

Let $\ell_{i,k,j}$ be the cross-entropy loss for token j in sentence $s_{i,k}$, and let $N = \sum_k n_k$ be the total token count. We define the standard cross-entropy loss

$$\mathcal{L}_{\text{CE}} = \frac{1}{N} \sum_{k=1}^K \sum_{j=1}^{n_k} \ell_{i,k,j} \quad (9)$$

and the weighted key-sentence loss

$$\mathcal{L}_{\text{key}} = \frac{1}{N} \sum_{k=1}^K \sum_{j=1}^{n_k} w_{i,k} \ell_{i,k,j} \quad (10)$$

Finally, the total TSL loss combines them with a sentence-ratio factor γ :

$$\mathcal{L}_{\text{TSL}} = \mathcal{L}_{\text{CE}} + \gamma \mathcal{L}_{\text{key}}. \quad (11)$$

This formulation amplifies gradients for infrequent yet clinically critical sentences while ensuring stable training by bounding all token weights.

Contextual Evidence Filter

Adaptive Prior Filter begins by splitting each available prior report y_i^{pri1} and y_i^{pri2} into individual sentences $\mathcal{S}_i = \text{Split}(y_i^{\text{pri1}}) \cup \text{Split}(y_i^{\text{pri2}}) = \{s_{i,1}, \dots, s_{i,K_i}\}$, where \mathcal{S}_i is the set of all extracted sentences. Each $s_{i,k}$ is classified by CheXbert(Smit et al. 2020) into a 14-dimensional label vector $\mathbf{y}_{i,k} \in \{-1, 0, 1, 2\}^{14}$. Since the 14th category corresponds to “No Finding,” we focus only on the first 13 disease labels—retaining sentences where at least one of these 13 labels is positive. Inspired by PromptMRG(Jin et al. 2024), we leverage a CLIP model pretrained on the MIMIC training set (Endo et al. 2021) to compute image–text similarity. Each retained sentence $s_{i,k}$ is encoded via the CLIP text encoder into an embedding $t_{i,k}$, while the current multi-view images are encoded by the CLIP image encoder into a pooled image embedding v_i ; their cosine similarity is then computed as

$$\text{sim}_{i,k} = \frac{v_i^\top t_{i,k}}{\|v_i\| \|t_{i,k}\|} \quad (12)$$

Rather than using a single static cutoff, we leverage the fact that the most recent prior report more reliably reflects current disease status. Therefore, for findings that appear in the older report but vanish in the latest one, we raise the threshold—using τ_{high}^+ —to aggressively prune any potentially outdated or irrelevant sentences (see Algorithm 1 in the Appendix). Formally, for each candidate sentence, we compute its CLIP similarity $\text{sim}_{i,k}$ with the current image and retain it only if

$$\text{sim}_{i,k} \geq \tau_{\text{risk}}, \quad (13)$$

where τ_{risk} is set to the higher threshold τ_{high}^+ for vanished findings. This scheme focuses on high-evidence content and actively removes stale information.

Experiments

Datasets

1) **MIMIC-CXR** (Johnson et al. 2019) is a large-scale, publicly available dataset of paired chest radiographs and free-text reports, organized chronologically per patient to support

Dataset	Model	Venue	Input	NLG metrics						CE metrics		
				B-1	B-2	B-3	B-4	R-L	MTR	P	R	F1
MIMIC-CXR	DCL	CVPR'23	Sin	—	—	—	0.109	0.284	0.150	0.471	0.352	0.471
	MET	CVPR'23	Sin	0.386	0.250	0.169	0.124	0.291	0.152	0.364	0.309	0.311
	KiUT	CVPR'23	Sin	0.382	0.247	0.177	0.135	0.299	0.158	0.523	0.410	0.460
	CoFE	ECCV'24	Sin	—	—	—	0.125	0.304	0.176	0.489	0.370	0.405
	MAN	AAAI'24	Sin	0.396	0.244	0.162	0.115	0.274	0.151	0.411	0.398	0.389
	B-LLM	AAAI'24	Sin	0.402	0.262	0.180	0.128	0.291	0.175	0.465	<u>0.482</u>	0.473
	ATL-CA	TMM'25	Sin-Lon	0.388	0.265	0.196	0.153	<u>0.321</u>	0.161	0.473	0.366	0.377
	HC-LLM	AAAI'25	Sin-Lon	0.404	0.260	0.178	0.128	0.287	0.160	0.417	0.357	0.357
	CXPMRG	CVPR'25	Sin-Lon	<u>0.422</u>	0.268	0.184	0.133	0.289	0.167	—	—	—
	MLRG	CVPR'25	Mul-Lon	0.411	<u>0.277</u>	<u>0.204</u>	<u>0.158</u>	0.320	0.176	0.549	0.468	<u>0.505</u>
Ours	—	Mul-Lon	0.432	0.292	0.216	0.170	0.328	0.196	<u>0.527</u>	0.516	0.521	

Table 1: Comparison with state-of-the-art on MIMIC-CXR. The *Input* column denotes the model inputs: *sin* indicates a single-view setting, *sin-lon* represents a single-view with longitudinal (historical) information, and *mul-lon* refers to a multi-view with longitudinal information. The best results are in **bold** while the second-highest are underlined.

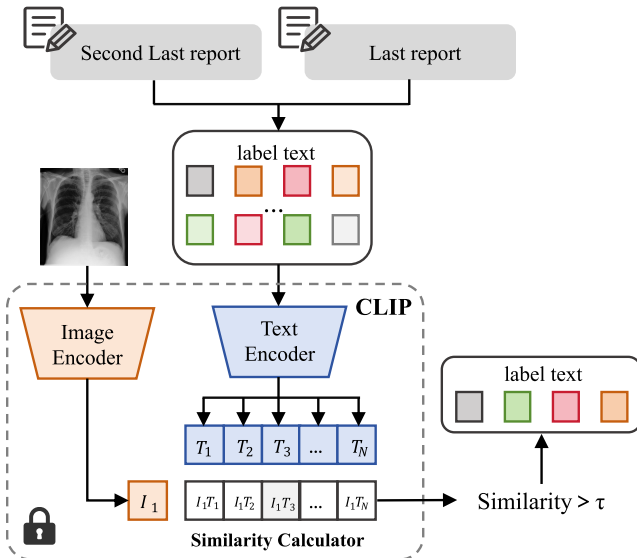


Figure 3: Architecture of Clip Model for Prior Filtering.

multi-view and longitudinal modeling.

2) IU-Xray (Demner-Fushman et al. 2015) is also widely used for MRG evaluation, which contains 2,955 samples in total after preprocessing. For both datasets, we use the official training/validation/test splits and treat each report’s “Findings” section as the reference text(Ramesh, Chi, and Rajpurkar 2022; Jin et al. 2024; Liu et al. 2025a).

Evaluation Metrics

We assess model performance using both natural language generation (NLG) metrics and clinical efficacy (CE) metrics.

For NLG, we report BLEU (Papineni et al. 2002), METEOR (Denkowski and Lavie 2011) and ROUGE-L (Lin 2004). To measure clinical accuracy, we follow Nicolson et al. (Jin et al. 2024) and convert each generated report into a 14-label disease vector via CheXbert, then compute precision, recall and F1 on these labels.

Implementation Details

For all experiments, we adopt XraySigLIP (Chen et al. 2024b) as our frozen image encoder and Vicuna-7B v1.5 (Chiang et al. 2023) as our text decoder. We set the number of learnable disease query tokens to $N_q = 128$, the similarity threshold $\tau = 0.22$ (see Appendix Figure A1 for details), the imbalance loss weight $\lambda = 2$, and the tier thresholds $T_1 = 20000$, $T_2 = 8000$.

Training proceeds in two stages,

1. **Frontal-only pretraining** Freeze both XraySigLIP and Vicuna, remove all prior-study and lateral inputs, and train only the FAVR module on frontal images for 2 epochs. This stage focuses on learning rich frontal representations to guide later fusion.
2. **Full fine-tuning with LoRA** Keep XraySigLIP frozen, enable LoRA adapters in Vicuna, and re-introduce all modules (FAVR, CEF, TSL) along with lateral images and prior-study inputs. The entire pipeline—including lateral-view resampling, adaptive prior filtering, and token-level amplification—is then jointly optimized for 4 epochs.

Results

We compare our model with ten SOTA methods—DCL(Li et al. 2023), MET(Wang et al. 2023b), KiUT(Huang, Zhang, and Zhang 2023), CoFE(Li et al. 2024), MAN(Shen et al.

Modules			NLG metrics				CE metrics		
FAVR	CEF	TSL	B-1	B-4	R-L	MTR	P	R	F1
✗	✗	✗	0.398	0.156	0.298	0.161	0.485	0.398	0.431
✓	✗	✗	0.434	0.163	0.321	0.189	0.523	0.421	0.463
✓	✗	✓	0.431	0.157	0.318	0.184	0.506	0.501	0.503
✓	✓	✗	0.435	0.170	0.326	0.193	0.540	0.425	0.475
✓	✓	✓	0.432	0.170	0.328	0.196	0.527	0.516	0.521

Table 2: Ablation study on MIMIC-CXR (NLG: B-1, B-4, R-L, MTR; CE: P, R, F1). The best results are in **bold**.

2024), B-LLM(Liu et al. 2024a), ATL-CA(Mei et al. 2025), HC-LLM(Liu et al. 2025b), CXPMRG(Wang et al. 2025b), and MLRG(Liu et al. 2025a)—on MIMIC-CXR . As shown in Table 1, SURE-Med achieves the top scores on all NLG metrics (BLEU-1 through METEOR and ROUGE-L) and leads in overall F1 (0.520 vs. 0.505 for MLRG). With respect to recall, our model achieves a 5% percentage-point absolute improvement over the recent work MLRG. To evaluate the reliability of our model, we did not perform any training on IU-Xray. Instead, we directly tested the model—trained solely on MIMIC-CXR—on the entire IU-Xray set, with a primary focus on CE metrics. This allows us to assess whether the model can reliably capture disease findings across different report formats. As shown in Table 3, even

Dataset	Model	CE metrics		
		P	R	F1
IU-Xray	MET	0.153	0.145	0.145
	DCL	0.168	0.167	0.162
	B-LLM	0.193	0.183	0.194
	MAN	0.217	0.192	0.203
	Ours	0.456	0.484	0.431

Table 3: Clinical efficacy (CE) metrics on IU-Xray. The best results are in **bold**.

without any fine-tuning on the IU-Xray dataset, our model achieves the highest precision, recall, and F1 score across all compared methods. This demonstrates its strong cross-dataset generalization and robustness: the representations learned on MIMIC-CXR effectively transfer to a different reporting style and pathology distribution, confirming that SURE-Med reliably captures clinically relevant features and scales to diverse real-world settings.

Ablation Analysis

To verify the effectiveness of each module, we do ablation study on MIMIC test set, which is shown in Table 2. The baseline model—devoid of FAVR, CEF, and TSL—produces only modest report quality and an F1 of about 0.431. Introducing FAVR equips the network with multi-view feature reconstruction, enriching spatial context and substantially boosting both fluency and precision. When TSL is added atop FAVR, we observe a further boost in lesion recall and cross-modal alignment—an improvement we

attribute to TSL’s mechanism of encouraging the model to emphasize critical clinical phrases. However, this focus on key findings slightly reduces BLEU-1, likely because prioritizing essential sentences can introduce minor disruptions in overall fluency. Similarly, when we add CEF on top of FAVR alone, precision increases by 1.7% and text-generation metrics also see modest gains, demonstrating that CEF brings a positive effect in screening past disease mentions. When all three modules are combined, the model achieves the most balanced performance, delivering strong coherence, diversity, and classification robustness. Although precision does not reach its absolute peak in this configuration, recall climbs to its highest level—underscoring TSL’s focus on critical clinical sentences. At the same time, precision remains higher than in the FAVR + TSL setting alone, confirming the complementary benefit that CEF brings to the overall system.

Case study

We present two qualitative examples in Figure 4 to demonstrate the superiority of SURE-Med over the baseline. In Example 1, our View-Repair module correctly relabels an originally “UNK” frontal view as AP and aligns it with the lateral image; the baseline, lacking view context, misses the mild cardiomegaly (purple highlight) and even omits critical descriptions of the lungs (red highlight). In Example 2, CEF removes the outdated Fracture history while correctly retaining Support Devices, enabling SURE-Med to accurately report unchanged support device placement (red highlight), whereas the baseline erroneously hallucinates a resolved hydropneumothorax cavity (underlined) and neglects to mention the unremarkable status of the left hemithorax—an observation correctly captured by both the ground truth and our model (blue highlight). Moreover, our TSL module boosts the model’s focus on critical disease terms, helping it correctly identify conditions such as cardiomegaly and atelectasis while avoiding false positives. By restoring correct view labels, pruning stale priors, and amplifying key diagnostic tokens, SURE-Med faithfully captures true findings, suppresses spurious details, and produces clearer, more clinically reliable reports.

Disease Imbalance

To assess the effectiveness of the TSL module’s imbalance handling, we run two experiments: one using the full TSL model (with class-weighting enabled) and one with

  <p>Original view: UNK Original view: UNK View-Repair:AP View-Repair:LATERAL No prior information</p>	<p>Reference report: Both lungs are well expanded and clear. There are no lung opacities concerning for pneumonia or pulmonary edema. Heart size is mildly enlarged and stable since _____. Mediastinal and hilar contours are unchanged. There is no pleural effusion or pneumothorax.</p> <p>MLRG: Frontal and lateral chest radiographs were obtained. no focal consolidation, pleural effusion, pneumothorax, or pulmonary edema is seen. the heart size is normal, mediastinal and hilar contours are normal. no bony abnormality is detected.</p> <p>Ours: Compared with the prior study, the cardiac silhouette appears mildly enlarged with no clear evidence of pleural effusion. Mediastinal and hilar contours are unremarkable. Both lungs are clear. This finding might indicate early pericardial effusion. No acute focal consolidation is observed.</p>						
  <p>PA Lateral CEF</p> <table border="1"> <thead> <tr> <th>Second</th> <th>Last</th> <th>Filter</th> </tr> </thead> <tbody> <tr> <td>Fracture</td> <td>No finding</td> <td>No finding</td> </tr> </tbody> </table>	Second	Last	Filter	Fracture	No finding	No finding	<p>Reference report: PA and lateral chest views were obtained with patient in upright position. The previously described right-sided chest tube remains in unchanged position. No pneumothorax has developed and there is no evidence of significantly increased pleural densities during this interval. The right-sided chest wall emphysema described earlier has regressed. No new abnormalities are seen. Left-sided hemithorax is unremarkable.</p> <p>MLRG: Pa and lateral chest views were obtained with patient in upright position. the right-sided chest tube remains in unchanged position and terminates in the right apical area. the previously described remaining small hydropneumothorax cavity has now resolved up to 2 cm. the remaining right-sided chest tube remains in unchanged position. no pneumothorax has developed.</p> <p>Ours: PA and lateral chest views were obtained with patient in upright position. Right-sided chest tube remains in unchanged position. No pneumothorax has developed during the latest examination interval. The previously described right-sided pleural thickenings and scar formations in right apical area remain unchanged. Left-sided hemithorax is unremarkable. Thoracic aorta unremarkable. No new pulmonary infiltrates are identified.</p>
Second	Last	Filter					
Fracture	No finding	No finding					

Figure 4: Generated reports examples on the MIMIC-CXR test set. Each sentence in the reference report is marked with a distinct color to show its correspondence in the generated report, and the matching passages in the generated report are highlighted using the same color. Failure descriptions are in underlined.

that weighting removed (assigning every class its maximum weight). We then compared per-class F1 scores across both settings. Introducing class-weighting led to dramatic F1 improvements for low-sample conditions—such as Pleural Other and Consolidation—where scores more than doubled, demonstrating that imbalance-aware weighting can substantially alleviate performance bottlenecks caused by scarce data. By contrast, for high-frequency conditions—such as Cardiomegaly, Support Devices, and Lung Opacity—the gains were minimal or even slightly negative, indicating that the marginal benefit of class weighting diminishes as sample size grows. We also evaluated standard NLG metrics; those results are presented in Table A3 of the Appendix.

Dynamic Threshold

Setting	B-1	B-4	R-L	P	R	F1
None	0.431	0.167	0.321	0.506	0.501	0.503
Fixed	0.431	0.168	0.326	0.515	0.518	0.517
Dynamic	0.432	0.170	0.328	0.527	0.516	0.521

Table 4: Ablation results on history filtering.

To assess the impact of our sentence-level history filtering strategy, we compare the Fixed setting (using a constant similarity threshold) with the Dynamic variant, which adaptively adjusts the threshold based on label progression. As shown in Table 4, the Dynamic strategy yields marginal improvements in text generation metrics, suggesting slightly better alignment with reference reports. More notably, Dynamic leads to a further boost in precision, rising from 0.515 to 0.527, indicating that dynamically filtered sentences are more semantically relevant and less noisy. Although recall

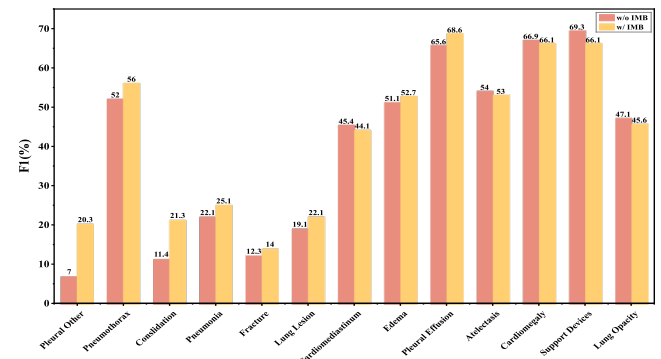


Figure 5: Comparison of the F1 score (%) across diseases between the method with and without IMB. The diseases are sorted in ascending order of their training sample counts.

slightly decreases, the overall F1 score still improves from 0.517 to 0.521, suggesting that the precision gain outweighs the minor recall drop. These results demonstrate that dynamic thresholding enhances the ability to preserve clinically meaningful content while aggressively filtering out irrelevant or outdated findings.

Conclusion and Future Work

In this work, we introduce SURE-Med, a unified framework that simultaneously repairs view labels, applies token-level imbalance augmentation, and filters semantically aligned historical sentences to address view noise, long-tail pathology imbalance, and hallucinations in chest X-ray report generation. On MIMIC-CXR and IU-Xray, our model achieves significant improvements in both language metrics and clinical efficacy, setting a new state-of-the-art. Looking ahead,

we will extend this approach to other imaging modalities (CT, MRI), leverage self-supervised pretraining on large radiology corpora to enhance domain representations, and integrate uncertainty estimation for interactive, confidence-aware report refinement—bridging the gap between research prototypes and routine clinical practice.

References

Amorosa, J. K.; Bramwit, M. P.; Mohammed, T.-L. H.; Reddy, G. P.; Brown, K.; Dyer, D. S.; Ginsburg, M. E.; Heitkamp, D. E.; Jeudy, J.; Kirsch, J.; et al. 2013. ACR appropriateness criteria routine chest radiographs in intensive care unit patients. *Journal of the American College of Radiology*, 10(3): 170–174.

Bannur, S.; Bouzid, K.; Castro, D. C.; Schwaighofer, A.; Thieme, A.; Bond-Taylor, S.; Ilse, M.; Pérez-García, F.; Salvatelli, V.; Sharma, H.; Meissen, F.; Ranjit, M.; Srivastav, S.; Gong, J.; Codella, N. C. F.; Falck, F.; Oktay, O.; Lungren, M. P.; Wetscherek, M. T.; Alvarez-Valle, J.; and Hyland, S. L. 2024. MAIRA-2: Grounded Radiology Report Generation. arXiv:2406.04449.

Broder, J. 2011. Imaging the chest: the chest radiograph. *Diagnostic imaging for the emergency physician*, 185.

Chawla, N. V.; Bowyer, K. W.; Hall, L. O.; and Kegelmeyer, W. P. 2002. SMOTE: synthetic minority over-sampling technique. *Journal of artificial intelligence research*, 16: 321–357.

Chen, W.; Shen, L.; Lin, J.; Luo, J.; Li, X.; and Yuan, Y. 2024a. Fine-Grained Image-Text Alignment in Medical Imaging Enables Explainable Cyclic Image-Report Generation. In *Proceedings of the 62nd Annual Meeting of the Association for Computational Linguistics (Volume 1: Long Papers)*, 9494–9509.

Chen, Z.; Shen, Y.; Song, Y.; and Wan, X. 2021. Cross-modal Memory Networks for Radiology Report Generation. In *Proceedings of the 59th Annual Meeting of the Association for Computational Linguistics and the 11th International Joint Conference on Natural Language Processing (Volume 1: Long Papers)*, 5904–5914.

Chen, Z.; Song, Y.; Chang, T.-H.; and Wan, X. 2020. Generating Radiology Reports via Memory-driven Transformer. In *Proceedings of the 2020 Conference on Empirical Methods in Natural Language Processing (EMNLP)*, 1439–1449.

Chen, Z.; Varma, M.; Delbrouck, J.-B.; Paschali, M.; Blankemeier, L.; Van Veen, D.; Valanarasu, J. M. J.; Youssef, A.; Cohen, J. P.; Reis, E. P.; et al. 2024b. CheX-agent: Towards a Foundation Model for Chest X-Ray Interpretation. In *AAAI 2024 Spring Symposium on Clinical Foundation Models*.

Chiang, W.-L.; Li, Z.; Lin, Z.; Sheng, Y.; Wu, Z.; Zhang, H.; Zheng, L.; Zhuang, S.; Zhuang, Y.; Gonzalez, J. E.; et al. 2023. Vicuna: An open-source chatbot impressing gpt-4 with 90%* chatgpt quality. See <https://vicuna.lmsys.org> (accessed 14 April 2023), 2(3): 6.

Cui, Y.; Jia, M.; Lin, T.-Y.; Song, Y.; and Belongie, S. 2019. Class-balanced loss based on effective number of samples. In *Proceedings of the IEEE/CVF conference on computer vision and pattern recognition*, 9268–9277.

Demner-Fushman, D.; Kohli, M. D.; Rosenman, M. B.; Shooshan, S. E.; Rodriguez, L.; Antani, S.; Thoma, G. R.; and McDonald, C. J. 2015. Preparing a collection of radiology examinations for distribution and retrieval. *Journal of the American Medical Informatics Association*, 23(2): 304–310.

Denkowski, M.; and Lavie, A. 2011. Meteor 1.3: Automatic metric for reliable optimization and evaluation of machine translation systems. In *Proceedings of the sixth workshop on statistical machine translation*, 85–91.

Endo, M.; Krishnan, R.; Krishna, V.; Ng, A. Y.; and Rajpurkar, P. 2021. Retrieval-based chest x-ray report generation using a pre-trained contrastive language-image model. In *Machine Learning for Health*, 209–219. PMLR.

Gaggion, N.; Mosquera, C.; Mansilla, L.; Saidman, J. M.; Aineseder, M.; Milone, D. H.; and Ferrante, E. 2024. CheX-mask: a large-scale dataset of anatomical segmentation masks for multi-center chest x-ray images. *Scientific Data*, 11(1): 511.

Guo, Z.; Ma, J.; Xu, Y.; Wang, Y.; Wang, L.; and Chen, H. 2024. Histgen: Histopathology report generation via local-global feature encoding and cross-modal context interaction. In *International Conference on Medical Image Computing and Computer-Assisted Intervention*, 189–199. Springer.

Gupte, T.; Niljikar, M.; Gawali, M.; Kulkarni, V.; Kharat, A.; and Pant, A. 2021. Deep learning models for calculation of cardiothoracic ratio from chest radiographs for assisted diagnosis of cardiomegaly. In *2021 International conference on artificial intelligence, big data, computing and data communication systems (icABCD)*, 1–6. IEEE.

Hamamci, I. E.; Er, S.; and Menze, B. 2024. CT2Rep: Automated Radiology Report Generation for 3D Medical Imaging . In *proceedings of Medical Image Computing and Computer Assisted Intervention – MICCAI 2024*, volume LNCS 15012. Springer Nature Switzerland.

Holste, G.; Wang, S.; Jaiswal, A.; Yang, Y.; Lin, M.; Peng, Y.; and Wang, A. 2023. CXR-LT: multi-label long-tailed classification on chest X-rays. *PhysioNet*, 5(19): 1.

Huang, Z.; Zhang, X.; and Zhang, S. 2023. Kiut: Knowledge-injected u-transformer for radiology report generation. In *Proceedings of the IEEE/CVF conference on computer vision and pattern recognition*, 19809–19818.

Ji, J.; Luo, Y.; Sun, X.; Chen, F.; Luo, G.; Wu, Y.; Gao, Y.; and Ji, R. 2021. Improving image captioning by leveraging intra-and inter-layer global representation in transformer network. In *Proceedings of the AAAI conference on artificial intelligence*, volume 35, 1655–1663.

Jin, H.; Che, H.; Lin, Y.; and Chen, H. 2024. Promptmrg: Diagnosis-driven prompts for medical report generation. In *Proceedings of the AAAI Conference on Artificial Intelligence*, volume 38, 2607–2615.

Jing, B.; Xie, P.; and Xing, E. 2018. On the Automatic Generation of Medical Imaging Reports. In Gurevych, I.; and Miyao, Y., eds., *Proceedings of the 56th Annual Meeting of*

the Association for Computational Linguistics (Volume 1: Long Papers), 2577–2586. Melbourne, Australia: Association for Computational Linguistics.

Johnson, A. E.; Pollard, T. J.; Berkowitz, S. J.; Greenbaum, N. R.; Lungren, M. P.; Deng, C.-y.; Mark, R. G.; and Horng, S. 2019. MIMIC-CXR, a de-identified publicly available database of chest radiographs with free-text reports. *Scientific data*, 6(1): 317.

Li, M.; Lin, B.; Chen, Z.; Lin, H.; Liang, X.; and Chang, X. 2023. Dynamic graph enhanced contrastive learning for chest x-ray report generation. In *Proceedings of the IEEE/CVF Conference on Computer Vision and Pattern Recognition*, 3334–3343.

Li, M.; Lin, H.; Qiu, L.; Liang, X.; Chen, L.; Elsaddik, A.; and Chang, X. 2024. Contrastive learning with counterfactual explanations for radiology report generation. In *European Conference on Computer Vision*, 162–180. Springer.

Lin, C.-Y. 2004. Rouge: A package for automatic evaluation of summaries. In *Text summarization branches out*, 74–81.

Lin, T.-Y.; Goyal, P.; Girshick, R.; He, K.; and Dollár, P. 2017. Focal loss for dense object detection. In *Proceedings of the IEEE international conference on computer vision*, 2980–2988.

Liu, C.; Tian, Y.; Chen, W.; Song, Y.; and Zhang, Y. 2024a. Bootstrapping large language models for radiology report generation. In *Proceedings of the AAAI Conference on Artificial Intelligence*, volume 38, 18635–18643.

Liu, K.; Ma, Z.; Kang, X.; Li, Y.; Xie, K.; Jiao, Z.; and Miao, Q. 2025a. Enhanced contrastive learning with multi-view longitudinal data for chest x-ray report generation. In *Proceedings of the Computer Vision and Pattern Recognition Conference*, 10348–10359.

Liu, K.; Ma, Z.; Kang, X.; Zhong, Z.; Jiao, Z.; Baird, G.; Bai, H.; and Miao, Q. 2024b. Structural Entities Extraction and Patient Indications Incorporation for Chest X-ray Report Generation. In *proceedings of Medical Image Computing and Computer Assisted Intervention – MICCAI 2024*, volume LNCS 15003. Springer Nature Switzerland.

Liu, K.; Ma, Z.; Liu, M.; Jiao, Z.; Kang, X.; Miao, Q.; and Xie, K. 2024c. Factual Serialization Enhancement: A Key Innovation for Chest X-ray Report Generation. *CoRR*.

Liu, R.; Li, M.; Zhao, S.; Chen, L.; Chang, X.; and Yao, L. 2024d. In-Context Learning for Zero-shot Medical Report Generation. In *ACM Multimedia 2024*.

Liu, R.; Li, M.; Zhao, S.; Chen, L.; Chang, X.; and Yao, L. 2024e. In-context learning for zero-shot medical report generation. In *Proceedings of the 32nd ACM international conference on multimedia*, 8721–8730.

Liu, T.; Wang, J.; Hu, Y.; Li, M.; Yi, J.; Chang, X.; Gao, J.; and Yin, B. 2025b. HC-LLM: Historical-constrained large language models for radiology report generation. In *Proceedings of the AAAI Conference on Artificial Intelligence*, volume 39, 5595–5603.

Lu, J.; Xiong, C.; Parikh, D.; and Socher, R. 2017. Knowing when to look: Adaptive attention via a visual sentinel for image captioning. In *Proceedings of the IEEE conference on computer vision and pattern recognition*, 375–383.

Mei, X.; Yang, L.; Gao, D.; Cai, X.; Han, J.; and Liu, T. 2025. Adaptive Medical Topic Learning for Enhanced Fine-Grained Cross-Modal Alignment in Medical Report Generation. *IEEE Transactions on Multimedia*, 1–12.

Nguyen, D.; Chen, C.; He, H.; and Tan, C. 2023. Pragmatic Radiology Report Generation. In Hegselmann, S.; Parziale, A.; Shanmugam, D.; Tang, S.; Asiedu, M. N.; Chang, S.; Hartvigsen, T.; and Singh, H., eds., *Proceedings of the 3rd Machine Learning for Health Symposium*, volume 225 of *Proceedings of Machine Learning Research*, 385–402. PMLR.

Nicolson, A.; Dowling, J.; Anderson, D.; and Koopman, B. 2024. Longitudinal data and a semantic similarity reward for chest X-ray report generation. *Informatics in Medicine Unlocked*, 50: 101585.

Nicolson, A.; Dowling, J.; and Koopman, B. 2023. Improving chest X-ray report generation by leveraging warm starting. *Artificial intelligence in medicine*, 144: 102633.

Papineni, K.; Roukos, S.; Ward, T.; and Zhu, W.-J. 2002. Bleu: a method for automatic evaluation of machine translation. In *Proceedings of the 40th annual meeting of the Association for Computational Linguistics*, 311–318.

Rajpurkar, P.; Irvin, J.; Zhu, K.; Yang, B.; Mehta, H.; Duan, T.; Ding, D.; Bagul, A.; Langlotz, C.; Shpanskaya, K.; et al. 2017. Chexnet: Radiologist-level pneumonia detection on chest x-rays with deep learning. *arXiv preprint arXiv:1711.05225*.

Ramesh, V.; Chi, N. A.; and Rajpurkar, P. 2022. Improving radiology report generation systems by removing hallucinated references to non-existent priors. In *Machine Learning for Health*, 456–473. PMLR.

Seo, H.; Lee, M.; Cheong, W.; Yoon, H.; Kim, S.; and Kang, M. 2023. Enhancing multi-label long-tailed classification on chest x-rays through ML-GCN augmentation. In *Proceedings of the IEEE/CVF international conference on computer vision*, 2747–2756.

Shen, H.; Pei, M.; Liu, J.; and Tian, Z. 2024. Automatic radiology reports generation via memory alignment network. In *Proceedings of the AAAI Conference on Artificial Intelligence*, volume 38, 4776–4783.

Simkus, P.; Gutierrez Gimeno, M.; Banisauskaite, A.; Norėikaite, J.; McCreavy, D.; Penha, D.; and Arzanauskaite, M. 2021. Limitations of cardiothoracic ratio derived from chest radiographs to predict real heart size: comparison with magnetic resonance imaging. *Insights into imaging*, 12(1): 158.

Smit, A.; Jain, S.; Rajpurkar, P.; Pareek, A.; Ng, A.; and Lungren, M. 2020. Combining Automatic Labelers and Expert Annotations for Accurate Radiology Report Labeling Using BERT. In Webber, B.; Cohn, T.; He, Y.; and Liu, Y., eds., *Proceedings of the 2020 Conference on Empirical Methods in Natural Language Processing (EMNLP)*, 1500–1519. Online: Association for Computational Linguistics.

Tanno, R.; Barrett, D. G. T.; Sellergren, A.; Ghaisas, S.; Dathathri, S.; See, A.; Welbl, J.; Lau, C.; Tu, T.; Azizi, S.; Singhal, K.; Schaekermann, M.; May, R.; Lee, R.; Man, S.; Mahdavi, S.; Ahmed, Z.; Matias, Y.; Barral, J.; Eslami, S. M. A.; and Ktena, I. 2025. Collaboration between clinicians

and vision-language models in radiology report generation. *Nature Medicine*, 31(2): 599–608.

Wang, F.; Du, S.; and Yu, L. 2024. Hergen: Elevating radiology report generation with longitudinal data. In *European Conference on Computer Vision*, 183–200. Springer.

Wang, F.; Du, S.; and Yu, L. 2025. HERGen: Elevating Radiology Report Generation with Longitudinal Data. In Leonardis, A.; Ricci, E.; Roth, S.; Russakovsky, O.; Sattler, T.; and Varol, G., eds., *Computer Vision – ECCV 2024*, 183–200. Cham: Springer Nature Switzerland. ISBN 978-3-031-73001-6.

Wang, X.; Figueiredo, G.; Li, R.; Zhang, W. E.; Chen, W.; and Chen, X. 2025a. A Survey of Deep Learning-based Radiology Report Generation Using Multimodal Data. arXiv:2405.12833.

Wang, X.; Wang, F.; Li, Y.; Ma, Q.; Wang, S.; Jiang, B.; and Tang, J. 2025b. Cxpmrg-bench: Pre-training and benchmarking for x-ray medical report generation on chexpert plus dataset. In *Proceedings of the Computer Vision and Pattern Recognition Conference*, 5123–5133.

Wang, Z.; Liu, L.; Wang, L.; and Zhou, L. 2023a. METransformer: Radiology Report Generation by Transformer with Multiple Learnable Expert Tokens. arXiv:2304.02211.

Wang, Z.; Liu, L.; Wang, L.; and Zhou, L. 2023b. ME-Transformer: Radiology Report Generation by Transformer with Multiple Learnable Expert Tokens. In *2023 IEEE/CVF Conference on Computer Vision and Pattern Recognition (CVPR)*, 11558–11567. IEEE.

Xu, K.; Ba, J.; Kiros, R.; Cho, K.; Courville, A.; Salakhudinov, R.; Zemel, R.; and Bengio, Y. 2015. Show, attend and tell: Neural image caption generation with visual attention. In *International conference on machine learning*, 2048–2057. PMLR.

Yang, J.; Su, B.; Zhao, W. X.; and Wen, J.-R. 2024. Unlocking the power of spatial and temporal information in medical multimodal pre-training. In *Proceedings of the 41st International Conference on Machine Learning*, 56382–56396.

Yang, S.; Wu, X.; Ge, S.; Zhou, S. K.; and Xiao, L. 2022. Knowledge matters: Chest radiology report generation with general and specific knowledge. *Medical image analysis*, 80: 102510.

Zeng, Z.; Zhang, H.; Lu, R.; Wang, D.; Chen, B.; and Wang, Z. 2023. Conzic: Controllable zero-shot image captioning by sampling-based polishing. In *Proceedings of the IEEE/CVF conference on computer vision and pattern recognition*, 23465–23476.

Zhang, K.; Yang, Y.; Yu, J.; Fan, J.; Jiang, H.; Huang, Q.; and Han, W. 2024. Attribute prototype-guided iterative scene graph for explainable radiology report generation. *IEEE Transactions on Medical Imaging*.

Zhang, Y.; Wang, X.; Xu, Z.; Yu, Q.; Yuille, A.; and Xu, D. 2020. When radiology report generation meets knowledge graph. In *Proceedings of the AAAI conference on artificial intelligence*, volume 34, 12910–12917.

Zhao, G.; Yan, Y.; and Zhao, Z. 2023. Normal-Abnormal Decoupling Memory for Medical Report Generation. In *Findings of the Association for Computational Linguistics: EMNLP 2023*, 1962–1977.